On vacancy and solute co-segregated η_1 interface in over-aged Al-Zn-Mg alloys

Yizi Ou[1], Yong Jiang[1], Yiren Wang[1], Zhengqing Liu[1]

Adrian Lervik[2], Randi Holmestad[2]

[1] State Key Laboratory for Powder Metallurgy, Key Laboratory for Nonferrous Metal Materials Science and Engineering (MOE), School of Materials Science and Engineering, Central South University, Changsha 410083, China

[2] Department of Physics, Norwegian University of Science and Technology, N-7491 Trondheim, Norway

Abstract

We represent a combined first-principles and scanning transmission electron microscopy (STEM) study of η_1 interfaces in an over-aged Al-Zn-Mg alloy. As one of the major η-MgZn$_2$ phase variant, η_1 tends to form highly coherent interfaces in Al, along with various unique solute segregation patterns on its interfacial layers. The interface phase diagram suggests either a Mg-rich or a Zn-rich interface, depending on the Zn chemical potential range. Further segregation calculations, however, strongly suggest the STEM Z-contrast imaged interface to be a vacancy and solute co-stabilized Mg-rich structure that is favored at relatively low Zn chemical potentials. Based on our experimental and calculation results, the profound thermodynamics origin of the η_1/Al interface and its intricate segregation behavior was clarified and described using a generalized structure model. The η_1/Al interface structure and segregation at higher Zn chemical potentials were also predicted for future experimental validation.

Keywords: Aluminum alloy; η-MgZn$_2$; precipitates; HAADF-STEM; Density Functional Theory (DFT)

* Corresponding author: Y. Jiang (yjiang@csu.edu.cn)

1. Introduction

Age-hardenable Al-Zn-Mg(-Cu) alloys are widely used for light-weight load-bearing structural components in aerospace and automotive applications, mainly due to their exceptional specific strength, good formability, and relatively-low production cost [1, 2]. The precipitation sequence during aging of Al-Zn-Mg(-Cu) alloys is generally described as: supersaturated solid solution (SSSS)→GP zones (GP-I and II)→η'→η [3-6]. The peak age-hardening is always achieved with a dense population of meta-stable η' as the major strengthening phase in Al matrix [7, 8]. A limitation with these alloys in their peak-aged conditions is the susceptibility to stress corrosion cracking (SCC) [9, 10]. In most applications, Al-Zn-Mg(-Cu) alloys have to be employed at the over-aged states with a sacrifice of strength, where stable η-precipitates becomes the dominating secondary phase in the matrix [3, 11].

The stable phase η-phase adapts a hexagonal C14 Laves structure (space group, $P6_3/mmc$) with a nominal composition of $MgZn_2$ [12, 13]. There exist at least thirteen variants of η with different orientation relationships in the matrix [6, 14-18]. Among them, $η_1$, $η_2$ and $η_4$ are the most commonly observed variants of η in over-aged Al-Zn-Mg(-Cu) alloys [3, 19]. We recently reported that $η_1$ can account for approximately 50% of the total number of nano-size hardening precipitates in an over-aged 7003 alloy [11]. Nevertheless, most past researches have been focused on plate-like $η_2$ which has been suggested to be the succeeding phase of η' due to their identical orientation relationship with the matrix [3, 4, 14, 20, 21]. For instance, the in-situ η'→$η_2$ transformation has been elucidated using high-resolution transmission electron microscopy (HRTEM) [14]. The other η variants are rarely studied.

η_1 may nucleate from pre-existing GP-zones [22] or precipitate directly out of the solid solution without aids of any transition phases [3]. The atomic stacking structure of η_1 phase turns out to be rather complex [15, 23, 24]. In addition to the regular R/R^{-1} stacking feature in its bulk structure as proposed by Marioara et al. [25], η_1 phase is often featured with some unique structural units on its interfaces which are presumably related to point defects, such as vacancies [15]. Chung et al. further suggested that η_1 tends to grow into a rod-like shape [15], due to their different lattice misfits along different interfacial facets. Recalling that η' and η_2 interfaces can be enriched with excess solute atoms due to interface segregation [25, 26], it is natural to believe that strong solute segregation might also occur at η_1 interfaces. Detailed knowledge about these interface details is an essential prerequisite for a full understanding of η_1 formation and its impact on the overall mechanical properties of the alloys. Various efforts have been recently devoted towards this aspect. Bendo et al. performed a high-angle annular dark-field (HAADF) scanning transmission electron microscopic (STEM) observation on η_1 phase, presenting a zig-zag structure of η_1/Al interfaces along the $\{001\}_{Al}$ habit plane [23]. A more recent combined HAADF-STEM and energy dispersive X-ray spectroscopy (EDXS) study further observed the co-segregation of Mg and Zn on the interface [27]. Nevertheless, many fundamentals are yet to be clarified, for instance, whether the co-segregation of Mg and Zn is an indispensable process for growing η_1 or a strong mechanism for stabilizing η_1. Hence, the origin of interface segregation and its significance on η_1 stabilities must be further elucidated.

In this study, we combined the HAADF-STEM characterization with density functional theory (DFT) calculations, to investigate the interface structure and segregation behaviors of η_1/Al at the atomic level. Based on the experimental orientation relation, various atomistic interface structures with different possible terminations were constructed and energetically optimized using DFT relaxation calculations. Based on these results, the interface phase diagram was constructed. The most feasible interface structure was determined by correlating with the experimental HAADF-STEM Z-contrast images. Possible segregation of excess quenched-in vacancies and solutes to the η_1/Al interface were further assessed by first-principles energetics. With the improved understanding of the interface, we were able to better interpret the experimental Z-contrast images, and further to develop a generalized structure model for η_1/Al interface by clarifying the profound roles of excess vacancies on solute segregation.

2. Methodology

2.1. Material

An AA7003 alloy with a composition of 5.56% Zn, 0.68% Mg, 0.01% Cu, 0.20% Fe, 0.11% Si, 0.17% Zr and 0.02% Ti (all in wt.%) was used. The alloy was extruded into hollow rectangular profiles with a dimension of 68×85 mm and a wall thickness of 2.4 mm. The profiles were thereafter solution treated at 480℃ for 30 min, followed by a water quench to room temperature. The samples were subsequently over-aged at 170℃ for 6 h (T7 temper).

2.2. Transmission electron microscopy

TEM specimens were prepared by grinding with SiC abrasive paper to ~100 μm foil thickness, punching into 3 mm discs, and subsequently electro-polishing using a Struers TenuPol-5 machine. An electrolyte made from 1/3 HNO$_3$ and 2/3 CH$_3$OH was used. It was kept at temperatures between -30 and -20℃ with an applied potential of 18 V. Precipitates were imaged in high-resolution HAADF-STEM using an image- and probe Cs-corrected JEOL ARM200CF operated at 200 kV, with a probe size of 0.08 nm, convergence semi-angle of 28 mrad and an inner collector angle of 48 mrad. High-resolution HAADF-STEM images were acquired using Smart Align, which involves acquiring a stack of successive low-dose images and afterwards aligning them to correct both rigid- and non-rigid scan distortions in the micrographs [28].

2.3. First-principles calculations

All structural relaxation and energetic calculations were performed using the density functional theory (DFT) code - VASP (Vienna Ab Initio Simulation Package) with periodic conditions and the plane-wave basis sets [29]. The electron-core interaction was described by the Blöchl projector augmented wave method (PAW) within the frozen-core approximation [30, 31]. Validation of the exchange-correlation (XC) functional was performed by fitting the energy-volume relation for fcc Al and hexagonal η_1 to the universal equation of state [32], to reproduce the experimental lattice constants. The tested XC-functionals included local density approximation (LDA) of Ceperley and Alder [33, 34], the generalized gradient approximation (GGA) of Perdew-Wang (PW91) [35] and the Perdew-Burke-Ernzerhof (PBE) functionals [36]. A sufficiently high energy cutoff of 350 eV was used for the plane-wave basis set

expansion. The PBE was finally adopted for its best prediction for lattice parameters of bulk η_1 (a=5.22 Å, b=8.53 Å), as compared to the experiment values of a=5.22 Å and c=8.57 Å [13]. For all the considered interface structures, we used a sandwich supercell of Al/η_1/Al consisting of a 9-layer Al block and a η_1 block with at least the same thickness. Full relaxation was performed on both the supercell volume and shape with a 3×2×1 Monkhorst-Pack k-mesh. The ground-state atomic structures were obtained by minimizing the Hellman-Feyman forces until the total forces on each ion were converged to within 0.02 eV/Å.

3. Results and discussion

3.1. HAADF-STEM observation

The over-aged treatment (T7) induces a dense distribution of η phases in the Al-Zn-Mg(-Cu) alloy samples with η_1 being the dominating variant, according to our previous study [11]. Figs. 1a and 1b show the atomic-resolution HAADF images of one typical plate-like η_1 nano-particle with a habit plane of $(001)_{Al}(//(10\bar{1}0)_{\eta_1})$, as viewed along $[1\bar{2}10]_{\eta_1}//[110]_{Al}$ and $[0001]_{\eta_1}//[1\bar{1}0]_{Al}$, respectively. The interface orientation relation can be thus easily identified as $(10\bar{1}0)[1\bar{2}10]_{\eta_1}//(001)[110]_{Al}$. On both ends of the η_1 particle, a coherent Zn-rich zig-zag layer (denoted as layer C) is clearly seen in Fig. 1a. Additionally, a row of pentagon-triangle (PT) structural units (comprising atoms on both layers A and B) are periodically stacked on top of layer C in Fig. 1a, which correspond to a row of small triangle (ST) structural units as viewed in the $[0001]_{\eta_1}(//[1\bar{1}0]_{Al})$ perspective in Fig. 1b. The spot brightness varies with atomic column sites. Almost all the atom-columns framed by PTs and STs show bright contrasts,

except the ones at the top-edge centers of the triangles of PTs (marked by orange arrows in Fig. 1a).

Recalling that the Z-contrast of an atom is proportional to the square of its atomic number Z, and hence on the Z-contrast images [37], both Zn and Cu atoms are similar in brightness while both Al and Mg atoms are also similar but less bright than Zn and Cu. Further considering the extremely low content of Cu (only 0.01 wt.%) in the studied alloy, one can deduce that each bright spot in Fig. 1 represents predominantly a Zn-rich atomic column. Meanwhile, on layer B, the pentagon centers of PTs and the middle sites between each ST pair are significantly darker. These findings agree generally well with the latest HAADF-STEM and EDXS observation on an Al-Zn-Mg alloy [27]. The very dark centers on layer B can be presumably attributed to vacancies (a hypotheses to be validated in the next section). The PTs and STs on layers A and B can be thus rationally presumed as unique vacancy+solute segregation patterns on η_1 interfaces. Besides PTs and STs, a periodic distribution of Zn-substitutional structural units (Zn_{Sub}, marked as doted blue squares) can be also observed on the interface as viewed along $[0001]_{\eta_1}//[1\bar{1}0]_{Al}$ in Fig. 1b. The periodicity of Zn_{Sub} units can be often related to interfacial strains imposed by the two mismatching half-lattices.
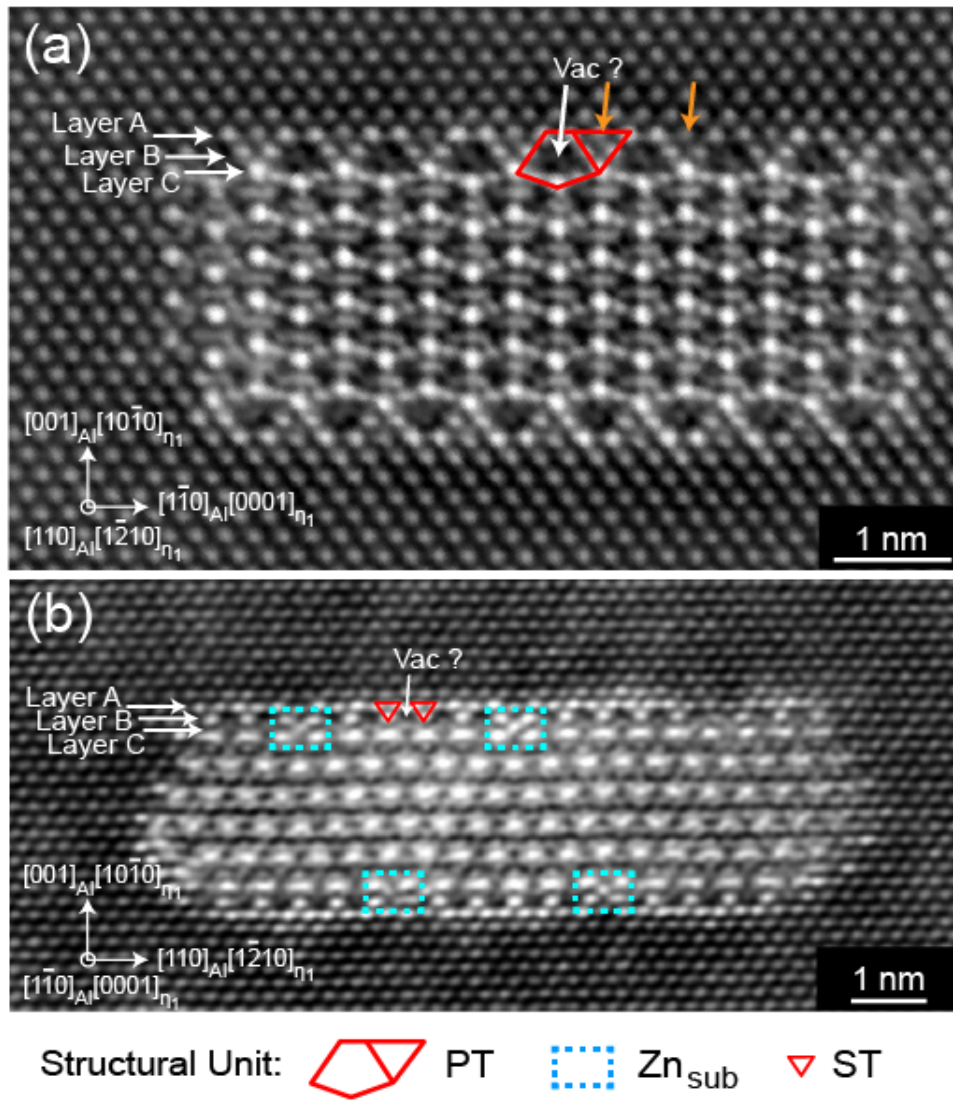
Fig. 1. HAADF-STEM micrographs of a typical η_1 nano-particle and its interfaces as viewed along (a) $[1\bar{2}10]_{\eta1}//[110]_{Al}$ and (b) $[0001]_{\eta1}//[1\bar{1}0]_{Al}$.

3.2. Interface structure modeling

Although the Z-contrast HAADF-STEM micrographs can provide many basic structural information of an interface, it is not sufficient to clarify such complex segregation behaviors as we suggested earlier. To face this challenge, we resorted to first-principles energetics calculations. For modeling the interface, we followed the experimental orientation relation and strained the η_1 lattice (which has lower elastic moduli than Al [38, 39]) to match with the

unstrained fcc-Al. That is, the η_1 lattice was stretched by 0.5% along the $[0001]_{\eta_1}(//[1\bar{1}0]_{Al})$ into the commensuration between $d(0001)_{\eta_1}$ and $3d(110)_{Al}$, and stretched by 8.7% along the $[1\bar{2}10]_{\eta_1}(//[110]_{Al})$ into the commensuration between $d(1\bar{2}10)_{\eta_1}$ and $d(110)_{Al}$. This arrangement is in agreement with various previous experimental characterizations [15, 27]. Again, the additional periodic Zn_{sub} units in Fig. 1b has great significance in alleviating the large commensuration strain (8.7%) along the $[0001]_{\eta_1}//[1\bar{1}0]_{Al}$ direction of the interface.

Fig. 2a schematically shows the orientation of η_1 phase in Al. By carefully checking the atomic stacking characters of the $\eta_1(10\bar{1}0)$ surface, a total of six different termination structures can be generated for the η_1/Al interface, namely the stoichiometric, Zn-rich I and II, and Mg-rich I, II and III, as shown in Fig. 2b. Besides the orientation relation and interfacial termination, interfacial atomic coordination may also have decisive influences on the local structure and chemistry of an interface [40-42]. Thus, for each termination, we further considered at least three types of interfacial coordination (not individually shown in Fig. 2b) depending on how to translate Al relative to η_1. DFT relaxation calculations were then performed on the resulting interface ensembles, to determine the most energy-favored structure of the η_1/Al.
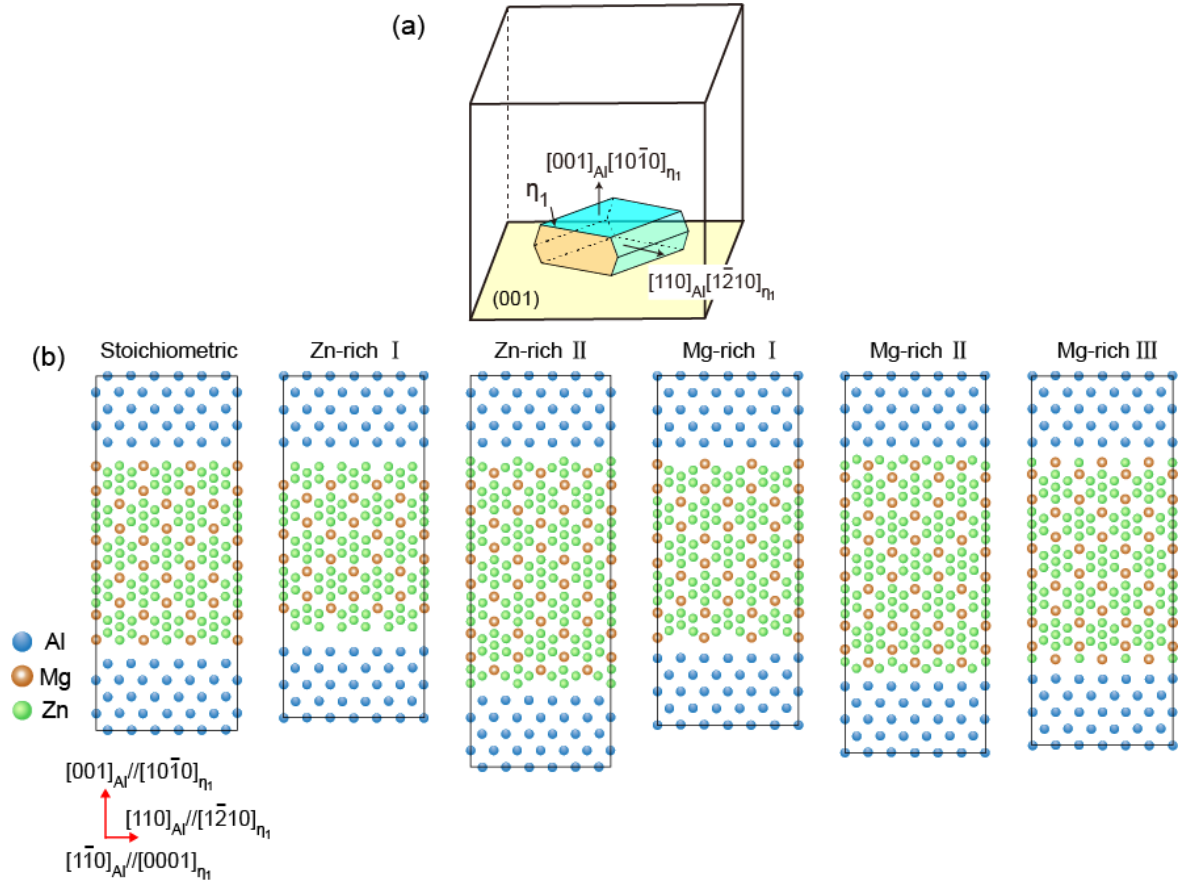
Fig. 2. (a) A 3D schematic showing the orientation relation of η_1 phases in Al. (b) The sandwich supercell models of η_1/Al interfaces with various different termination types, as viewed along the same direction of $[000\overline{1}]_{\eta1}(//[1\overline{1}0]_{Al})$.

3.3. Interface phase diagram

To determine the most feasible interface structure, we evaluated the formation energies of all the above interface ensembles under the thermodynamic equilibrium as [26].

$$\gamma = \frac{1}{2A}\left(E_{tot} - N_{Al}\mu_{Al} - N_{Mg}\mu_{Mg} - N_{Zn}\mu_{Zn} + P\Delta V - T\Delta S\right)$$

$$= \frac{1}{2A}\left[E_{tot} - N_{Al}\mu_{Al}^{\circ} - N_{Mg}\mu_{\eta}^{\circ} - \left(N_{Zn} - 2N_{Mg}\right)\mu_{Zn}^{\circ} - \left(N_{Zn} - 2N_{Mg}\right)\Delta\mu_{Zn}\right], \quad (1)$$

where γ is the interface energy, and E_{tot} is the total energy of a fully relaxed interface supercell. N_i and μ_i are the number and the chemical potential of element i (i=Al, Mg, or Zn),

respectively. The superscript o refers to the standard state. A is the cross-sectional area of the interface. ΔV is the volume change and ΔS is mainly the vibrational entropy change due to the interface formation. $\Delta \mu_i$ defines the excess chemical potential of element i, which measures the deviation of the real chemical potential μ_i at the interface from its standard state value, i.e. $\Delta \mu_i = \mu_i - \mu_i^o$. Please note that, under the ambient pressure and a practical aging temperature of 100~200°C, the last two terms, i.e. $P\Delta V$ and $T\Delta S$, are generally very small and can be neglected. Due to large cancellation in Eq. (1), all the energy terms E_{tot} and μ_i^o can be estimated by 0 K enthalpy calculations, as the first order approximation. The temperature dependence of interface energy would thus rely dominantly on $\Delta \mu_{Zn}$ ($= kT \ln a_{Zn}$). By definition, a_{Zn} is proportional to the Zn concentration through the activity coefficient γ_{Zn} which is also a function of temperature.

To ensure a stable interface, the chemical potential of Zn or Mg at interface must be limited to less than that in its pure bulk standard state, thus $\Delta \mu_{Zn} < 0$ and $\Delta \mu_{Mg} < 0$. Also, for the formation energy of bulk η_1 (MgZn$_2$) phase in Al, $\Delta H_f^\circ(\eta_1) = \Delta \mu_{Mg} + 2\Delta \mu_{Zn}$. Detailed deduction can be referred to one our previous work on η'/Al interfaces [21]. The reasonable varying range of $\Delta \mu_{Zn}$ can be thus determined as

$$\frac{1}{2}\Delta H_f^\circ(\eta_1) \leq \Delta \mu_{Zn} \leq 0 . \tag{2}$$

The formation energy of bulk phase η_1 is calculated to be $\Delta H_f^\circ(\eta_1) = -0.58$ eV per formula unit. Using Eqs. (1) and (2), all the interface energies can be calculated with respect to $\Delta \mu_{Zn}$ and the results are plotted in Fig. 3. Clearly, the stoichiometric interface energy is independent of $\Delta \mu_{Zn}$ due to its stoichiometric atomic ratio of Mg/Zn = 2. The Zn-rich interface energies

always decrease while the Mg-rich interface energies always increase as increasing $\Delta\mu_{Zn}$ (or μ_{Zn}). A lower interface energy generally predicts a higher interface stability. Hence, the Mg-rich II interface would dominate at the lower $\Delta\mu_{Zn}$ range of -0.3~-0.17 eV while the Zn-rich I interface dominate under $\Delta\mu_{Zn}$ >~-0.17 eV. All other suggested interfaces have higher formation energies and cannot favorably form in the alloys.

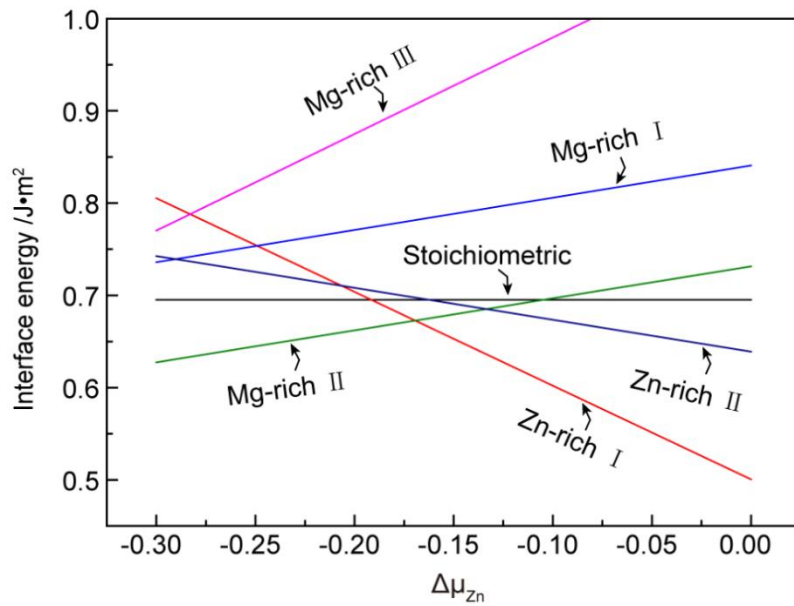Fig. 3 The calculated η_1/Al interface phase diagram to determine the most energy favorable interface structure under a given Zn chemical potential.

3.4. Interface structure determination

We further checked all the calculated interface structures with the experimental atomic-resolution structures for column-by-column alignment in Fig. 4. It is obvious that none of them can achieve a perfect match with the experimental structures simultaneously in both projected views of the $[1\bar{2}10]_{\eta 1}(//[110]_{Al})$ (Figs. 4a1-f1) and the $[0001]_{\eta 1}(//[1\bar{1}0]_{Al})$ (Figs. 4a2-f2). Nevertheless, the fully-relaxed Zn-rich I (Fig. 4a) and Mg-rich I structure (Fig. 4d) can reproduce the experimental structures to the most extent, except only the Z-contrast

discrepancies for those columns on layers A and B that obviously stem from vacancy and solute segregation. The Mg-rich II interface matches well the experimental image column-by-column along $[0001]_{\eta1}(//[1\bar{1}0]_{Al})$ (Fig. 4f2), but not at all along the $[1\bar{2}10]_{\eta1}(//[110]_{Al})$ (Fig. 4f1). For all other interface types, i.e. the Zn-rich II (Fig. 4b), the stoichiometric (Fig. 4c), and the Mg-rich II (Fig. 4e), the misalignment with the experimental structures are evidently too significant to be correct.
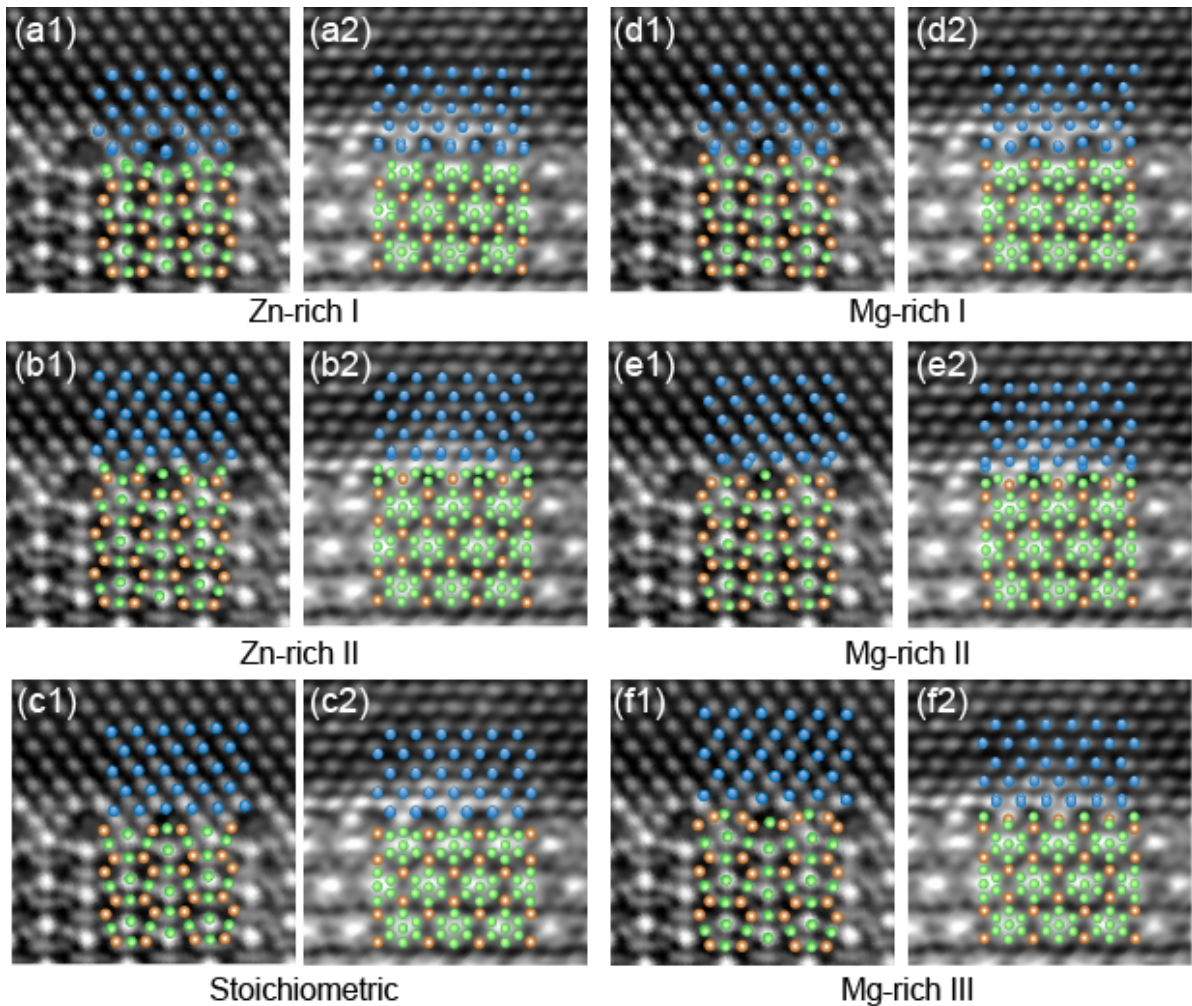

Fig. 4 Atomic superposition comparison between the HAADF-STEM imaged structures and the DFT-calculated interface structures with six different terminations, as viewed along the $[1\bar{2}10]_{\eta1}(//[110]_{Al})$ (a1-f1) and the $[0001]_{\eta1}(//[1\bar{1}0]_{Al})$ (a2-f2).

According to our predicted interface phase diagram, the Zn-rich I interface is the most energy-favored for $\Delta\mu_{Zn} > -0.17$ eV, but within the lower $\Delta\mu_{Zn}$ range, the Mg-rich I interface always has a higher formation energy than either the stoichiometric or the Mg-rich II interface. This strongly suggests that the segregation of vacancies and solutes to layers A and B have profound effects on the structural stability of the Mg-rich I interface, making it a possible candidate for the η_1/Al interface. A thorough investigation on interface segregation is thus highly necessary. The Mg-rich I interface as the structural model suggested by the interface phase diagram is not sufficient on its own.

3.5. Interface segregation of vacancies

In section 3.1, the periodically distributed dark column-sites on the interfacial layer B (indicated by white arrows in Fig. 1b) have been attributed to vacancies, and more specifically, to Al vacancies as suggested in Fig. 4. To validate this presumption, we first evaluate the vacancy formation on both the Zn-rich I and Mg-rich I interfaces. Considering that η_1 forms from a supersaturated solid solution with a high number of quenched-in vacancies, we regarded the vacancy formation as the consequence of interface segregation.

Interface segregation energy of a quenched-in vacancy (ΔE_{seg}^{Vac}) is then calculated as

$$\Delta E_{seg}^{Vac} = \left(E_{intf}^{Vac} - E_{intf}\right) - \left(E_{bulk}^{Vac} - E_{bulk}\right), \qquad (3)$$

where E_{intf}^{Vac} and E_{intf} are the total energies of the interface supercell with and without vacancies, and E_{bulk}^{Vac} and E_{bulk} are the total energies of a 4×4×4 fcc-Al supercell with and without vacancies, respectively. Both the two bulk energies were calculated using a 3×3×3 Monkhorst-Pack K-mesh. Negative ΔE_{seg}^{Vac} corresponds to an energetically favored vacancy

segregation from the bulk interior to the interface. Fig. 5 schematically show all the column sites possible for hosting segregated vacancies on the interfacial layer B of the Zn-rich I or the Mg-rich I interface. According to the local symmetry, there exist two non-equivalent types of atomic column sites (denoted as #1 and #2 in Fig. 5a1 and b1) as viewed along $[1\bar{2}10]_{\eta1}(//[110]_{Al})$ available for vacancies, each column consisting of two non-equivalent atom sites (denoted as I and II in Fig. 5a2 or b2) as viewed along the $[0001]_{\eta1}(//[1\bar{1}0]_{Al})$. Thus, there are a total of four candidate sites to be considered. Note that the PTs and STs have been highlighted in Fig. 5, to help compare with the experimental images in Fig. 1. The calculated vacancy segregation energies are given in Table 1.

It is clear from Table 1 that multiple sites at the η_1/Al interface demonstrate a negative ΔE_{seg}^{Vac}. An energy-favored vacancy segregation can help stabilize the interface. For single vacancy segregation, site 1-I is always the most preferred on both interfaces, which, however, is not consistent with the experimental Z-contrast image. On the other hand, for the cases of pair segregation, ΔE_{seg}^{Vac} at interfacial sites 1,2-I can be even more negative, indicating a strong affinity between the paired vacancies. In other words, vacancies can be more strongly trapped by pairing up at sites 1,2-I on both interfaces, no matter the interface termination type. This fits well with the dark column #2 and sites I, as well as the relatively low brightness of some columns #1 as observed in Fig. 1b. We can thus conclude that the segregation of excess quenched-in vacancies can strongly stabilize both interfaces, and especially the high-energy Mg-rich I interface with a much higher energy gain.

So far, solely based on our vacancy calculations, the observed interface structure in Fig. 1 still cannot be determined as Zn-rich I or Mg-rich I. Further solute segregation calculations on both interfaces are required, which, hopefully, can help us identify the interface type and clarify the even more intricate interaction between segregated vacancies and solutes at the interfaces.
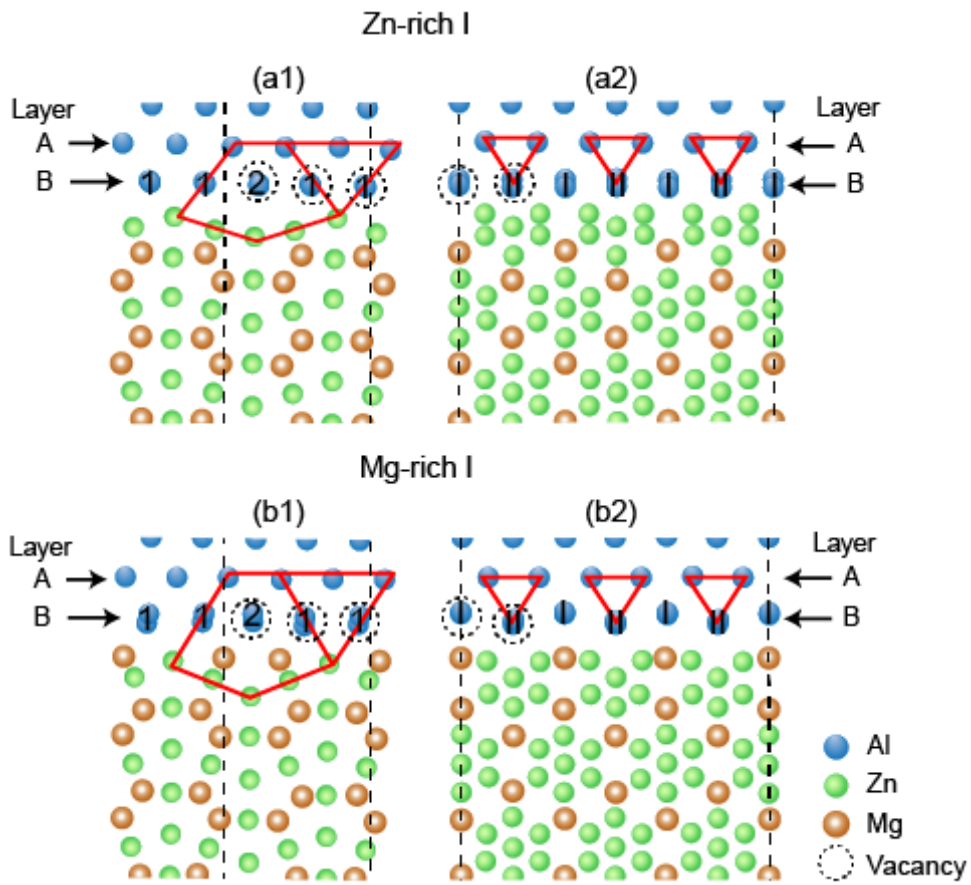

Fig. 5. The potential sites for vacancy segregation on the interfacial layers A and B of the η_1/Al interfaces: (a) the Zn-rich I, and (b) the Mg-rich I.

Table 1 Calculated vacancy segregation energies at the η_1/Al interface.

Segregated Vacancies	Segregated site	ΔE_{seg}^{Vac} (eV per vacancy)	
		Zn-rich I	Mg-rich I

	1-I	-0.189	-0.511
	2-I	-0.059	0.067
Single	1-II	-0.082	0.239
	2-II	0.154	0.179
Pairs in 1,2	1,2-I	-0.442	-0.622
	1,2-II	-0.131	0.951

3.6. Interface segregation of solutes

Besides vacancy segregation, the different Z contrasts observed on the interfacial layers A and B in Fig. 1 can also be possibly related to segregated solutes. Again, due to its extremely low concentration (~0.01 wt.% only) in our samples, the possible Cu segregation can be tentatively neglected. We thus proposed to examine the possibility of Zn and Mg segregation from inside the Al matrix to the vacancy-segregated interfaces, by calculating the solute segregation energy as

$$\Delta E_{seg}^X = \left(E_{intf}^{X+Vac} - E_{intf}^{Vac} \right) - \left(E_{bulk}^X - E_{bulk} \right). \tag{4}$$

Here E_{intf}^{X+Vac} and E_{intf}^{Vac} are the total energies of the vacancy-segregated interface supercell before and after single solute X (X=Zn or Mg) segregation. E_{bulk}^X is the total energy of a 4×4×4 fcc-Al supercell containing one single substitutional solute atom X. Both the two bulk energies (E_{bulk}^X and E_{bulk}) were calculated using a 3×3×3 Monkhorst-Pack K-mesh. Again, negative ΔE_{seg}^X corresponds to an energetically favorable solute segregation. The comparison of ΔE_{seg}^X among different sites reveals the formation preference of vacancy+solute segregation patterns at the interfaces.

According to the local symmetry, there are in total four types of non-equivalent atom-column sites (numbered from #1 to #4) available for solute segregation on the interfacial layers A and B, as shown in Fig. 6. The corresponding segregation energies were calculated and are compared. For the Zn-rich I interface, Zn can segregate to all the possible sites by ΔE_{seg}^{Zn} = -0.1~-0.2 eV per Zn atom, while Mg prefers site 2-II only, with a much higher ΔE_{seg}^{Mg} of -0.44 eV per Mg atom. For the Mg-rich I interface, Zn has nearly no segregation tendency while Mg still prefers site 2-II only, with ΔE_{seg}^{Mg} = -0.21 eV per Mg atom. This strongly suggests that the experimentally observed bright spots on layers A and B cannot possibly be expected for an Mg-rich I interface, or alternatively, the Z-contrast image in Fig. 1 can only possibly be attributed to a Zn-rich I interface.
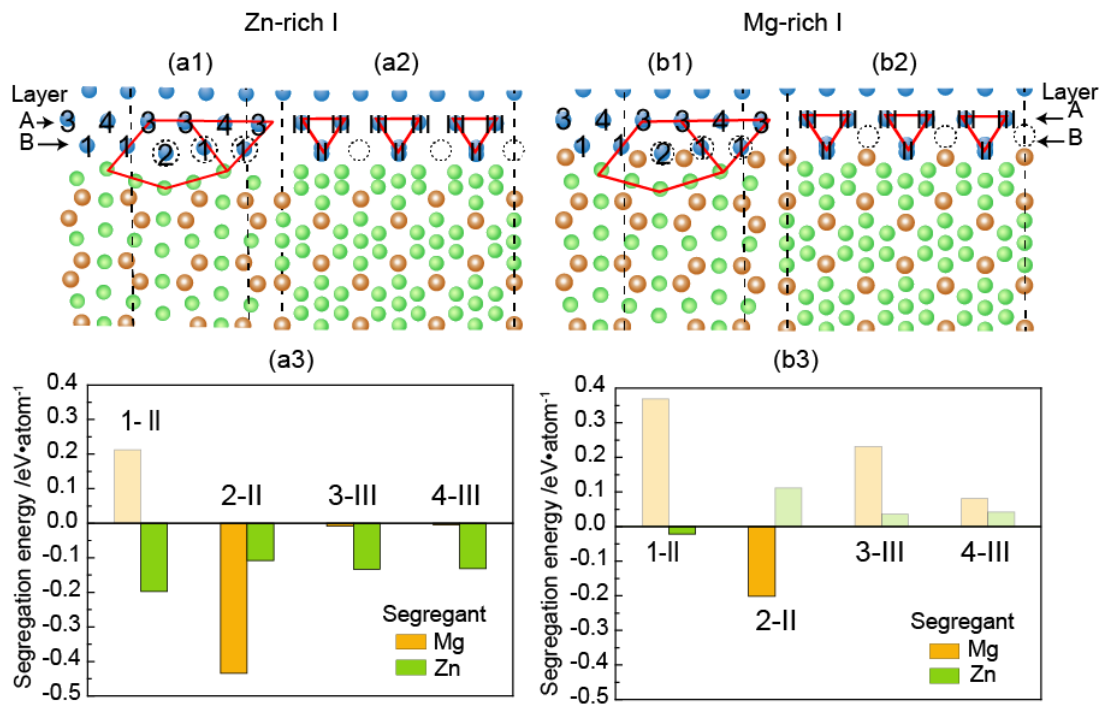

Fig. 6. The potential sites and the corresponding segregation energies for single Zn or Mg segregation on layers A and B of the η_1/Al interfaces: (a) the Zn-rich I, and (b) the Mg-rich I.

Nevertheless, the above calculations have been limited to single solute segregation. High-coverage solute segregation is highly worthy of studying. We thus further calculated the total energy reduction (ΔE) due to Zn and Mg co-segregation with respect to the resulting interface coverage. The co-segregation results on layer B are plotted in Fig. 7. Please note that on layer B, one monolayer (ML) denotes a full coverage of nine segregated solute atoms occupying all the numbered columns in Fig. 5a1 or 5b1, i.e. column #2 consists of all 2-II sites and the other two columns #1 consisting of all 1-II sites. Here in Fig. 7, "1/3 ML Mg" represents Mg substitution at all the 2-II sites, while "1/3 ML" and "2/3 ML Zn" represents one- and two-column substitution of Zn at 1-II sites, respectively. A general trend is revealed in Fig. 6 that, the total energies of both interfaces decrease consistently with the increasing coverage, until a full coverage of Zn and Mg is reached on layer B. On both the interfaces, the "1/3 ML" or "2/3 ML Zn" substitution at the 1-II sites would highlight the side edges of PTs on the experimental Z-contrast images, while the "1/3 ML Mg" substitution at all the 2-II sites would lead to a relatively dark contrast at the PT centers. These suggestions agree well with the observation in Fig. 1a. Also, the Zn-rich I interface can be stabilized more than the Mg-rich I interface by segregated solutes on the layer B.
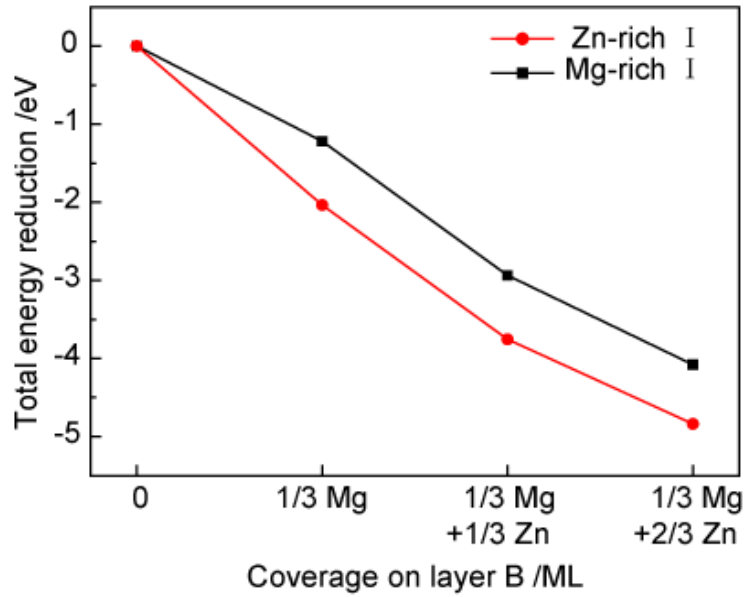
Fig. 7. Calculated total energy reduction due to high coverage solute segregation to layer B.

Upon a full coverage of layer B, further solute segregation to layer A was also calculated and the results are compared in Fig. 8. Please note that there exist only two types of non-equivalent atom-columns (#3 and #4) on layer A in Fig. 5a1 or 5a2, and both the two columns correspond to sites III in Fig. 5b1 or 5b2. Evidently, for both interfaces, Zn can segregate to all sites III on layer A with almost an equal tendency (by ΔE_{seg}^{Zn} = -0.16~0.18 eV per Zn atom), while Mg only prefers the 4-III sites (by ΔE_{seg}^{Mg} = -0.13~0.15 eV per Mg atom). Thus, the 3-III sites would appear to be brighter than the 4-III sites in the experimental Z-contrast images, which explains well the relatively dark top-edge centers of the triangles of PTs (as marked by orange arrows) in Fig. 1a. The stabilizing effects due to segregated solutes on layer A are very similar between the two interfaces.
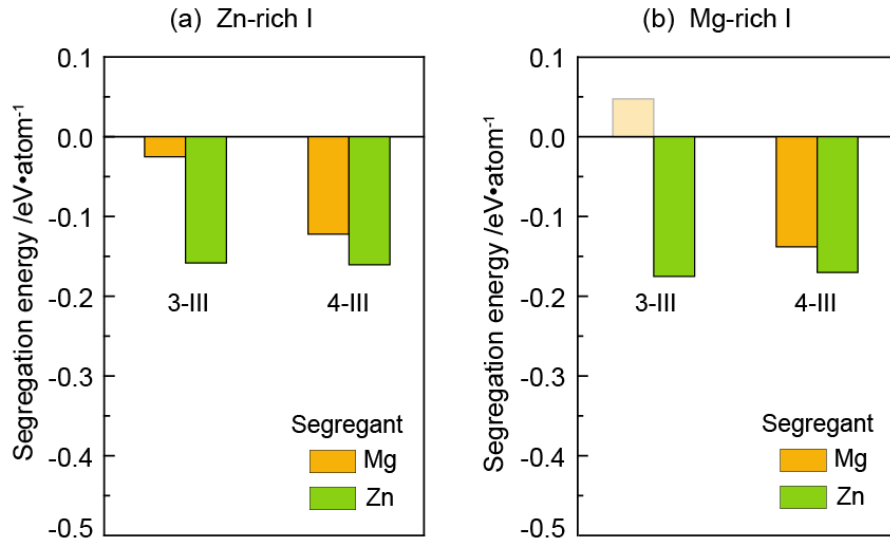
Fig. 8. Calculated segregation energies of solutes on layer A upon a full coverage of layer B.

3.7. Generalized interface structure model

As claimed in section 3.5, solely based on vacancy segregation calculations, the observed

structure in Fig. 1 cannot be determined as the Zn-rich I or the Mg-rich I. In section 3.6, the

attractive vacancy-solute affinity in bulk Al predicted by a previous theoretical study [43] has

been also demonstrated at the η_1/Al interfaces. Further solute segregation can greatly stabilize

both the two suggested interfaces, which might result in very similar Z-contrast images as

experimentally observed in Fig. 1. To double-check on this, we superimposed the

experimental HAADF-STEM images with the DFT-calculated structures of both interfaces

co-segregated with vacancies and solutes in Fig. 9. It is clear that, although segregation to the

two different interfaces might yield very similar vacancy+solute segregation patterns, the Mg-

rich I interface can achieve an nearly perfect matching with the experimental Z-contrast

images, simultaneously in both views along the $[1\bar{2}10]_{\eta 1}(//[110]_{Al})$ and the $[0001]_{\eta}//[1\bar{1}0]_{Al}$.

The Zn-rich I interface, however, misses the relatively dark sites 2-I (presumed as vacancy

sites) denoted by a red arrow in Fig. 9a2, which, as suggested in Fig. 9b2, can be partially occupied by up-shifted Mg atoms on the out-most layer C of η_1.

Based on all the results and discussions above, we can finally propose a generalized structure model for η_1/Al interfaces in Al-Zn-Mg(-Cu) alloys. That is, the η_1/Al interface is a vacancy+solute co-segregated Mg-rich I interface, which can be highly coherent in the Al matrix with an orientation relation of $(10\bar{1}0)_{\eta1}//(001)_{Al}$ and $[1\bar{2}10]_{\eta1}//[110]_{Al.}$ Without segregation, the most stable interface structure would be predicted by the interface phase diagram as the Mg-rich II or the Zn-rich I interface for low or high $\Delta\mu_{Zn}$ (or μ_{Zn}) values, respectively. Excess quenched-in vacancies and solutes diffuse and segregate to the interface during the over-aging time. Once reaching the interface, they can greatly stabilize the high-energy Mg-rich I interface, making it the most energetically feasible to form in the alloys. The real $\Delta\mu_{Zn}$ (or μ_{Zn}) is thus most likely to be within -0.3~-0.17 eV, which corresponds to the medium Zn concentration (~5.56 wt.%) of the alloys. Please note, the resulting structure in Fig. 9b can reproduce exactly the latest HAADF-STEM images interpreted by atomic-resolution EDXS in Ref. [27], and more importantly, our model with the developed understanding were based on the profound clarification of the thermodynamics origin of the η_1/Al interface and its intricate segregation behaviors. Moreover, a higher Zn concentration could lead to a higher $\Delta\mu_{Zn}$ (or μ_{Zn}) in favor of the formation of the Zn-rich I interface, which awaits future experimental evidence. The vacancy+solute segregated Zn-rich I interface structure has been also predicted in Fig. 9 for future reference. The impact of higher content of Cu is worthy of further exploration.
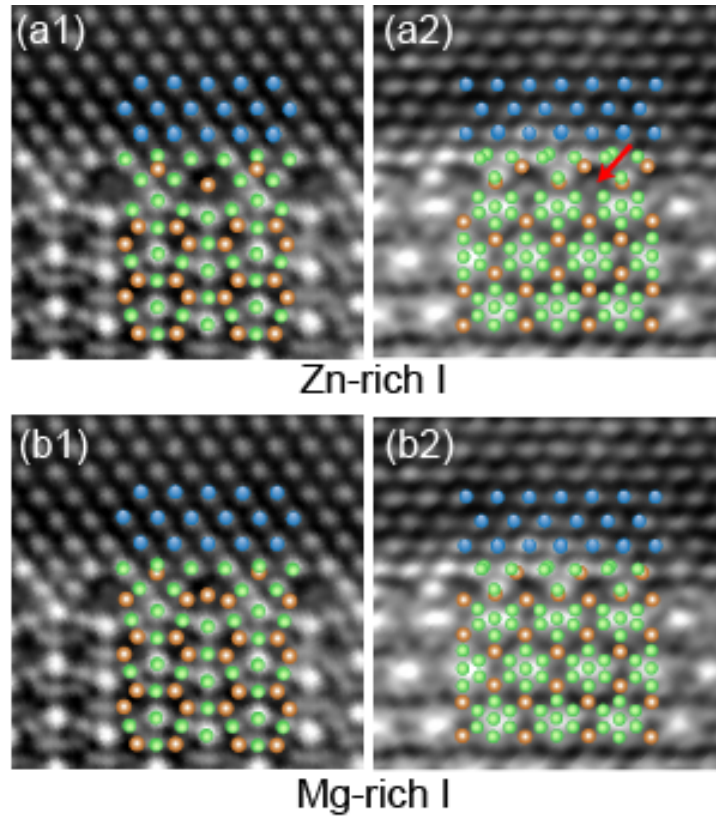
Fig. 9. Superimposition of the vacancy+solute co-stabilized interface structures with the HAADF-STEM Z-contrast images of the η_1/Al interface.

4. Conclusions

η_1 is known as one of the major η phase variant found in over-aged Al-Zn-Mg(-Cu) alloys. In this work, the η_1/Al interface structure has been thoroughly investigated by means of atomic-resolution HAADF-STEM analysis and first-principles DFT calculations. With the experimental orientation relation, various possible interface configurations were constructed and calculated to develop the interface phase diagram. Furthermore, these have been combined with vacancy and solute segregation calculations. We demonstrated the origin of unique segregation patterns at the interfacial layers, and their implication on interface stabilities were also discussed. The main findings can be summarized as follows:

(1) The η_1/Al interface is found to be highly coherent in Al matrix, with an orientation relation of $(10\bar{1}0)_{\eta1}//(001)_{Al}$ and $[1\bar{2}10]_{\eta1}//[110]_{Al}$. Periodic distribution of various unique segregation patterns is also observed along the two interfacial layers. The additional Zn-substitution structural units as periodically-observed along $[0001]_{\eta1}// [1\bar{1}0]_{Al}$ are likely caused in order to accommodate misfit strains.

(2) Without considering segregation, the calculated interface phase diagram predicts the most stable interface to be the Mg-rich II at lower $\Delta\mu_{Zn}$ values (-0.3~-0.17 eV) or the Zn-rich I at higher $\Delta\mu_{Zn}$ values (>~-0.17 eV). All other suggested interface structures have higher formation energies and thus cannot be favored to form in the alloys.

(3) However, the column-by-column alignment checking between the fully-relaxed interface structures with the experimental STEM images strongly suggested the η_1/Al interface to be either the Zn-rich I or the Mg-rich I. Further calculations revealed that excess quenched-in vacancies and solutes can strongly segregate to the two interfacial layers. The segregation can greatly stabilize both interface structures, and also produce various segregation patterns that are similar to the experimental STEM images.

(4) Combining our experimental observation and calculation results, the experimental Z-contrast images can be attributed to a vacancy and solute co-stabilized Mg-rich I interface, and the real $\Delta\mu_{Zn}$ range can be thus deduced as within -0.3~-0.17 eV, corresponding to the medium Zn concentration (~5.56 wt.%) of the alloy.

(5) Our model and its interpretation were developed with the profound understanding of the thermodynamics origin of the η_1/Al interface under intricate segregation effects. A higher

Zn concentration could lead to a higher $\Delta\mu_{Zn}$ (or μ_{Zn}) in favor of the formation of the Zn-rich I interface. The vacancy and solute stabilized Zn-rich I interface structure has been also predicted for future experimental validation.

References

[1] J.C. Williams, E.A. Starke, Progress in structural materials for aerospace systems, Acta Mater. 51(19) (2003) 5775-5799.

[2] T. Dursun, C. Soutis, Recent developments in advanced aircraft aluminium alloys, Mater. Des. 56 (2014) 862-871.

[3] J. Gjønnes, C.J. Simensen, An electron microscope investigation of the microstructure in an aluminium-zinc-magnesium alloy, Acta Metall. Mater. 18 (1970) 881-890.

[4] S.P. Ringer, K. Hono, Microstructural evolution and age hardening in aluminium alloys: atom probe field-ion microscopy and transmission electron micro-scopy studies, Mater. Char. 44 (2000) 101-131.

[5] S.J. Andersen, C.D. Marioara, J. Friis, S. Wenner, R. Holmestad, Precipitates in aluminium alloys, Adv. Phys. X 3(1) (2018) 790-813.

[6] L.K. Berg, J. Gjønnes, V. Hansen, X.Z. Li, M. Knutson-Wedel, G. Waterloo, D.Schryvers, L.R. Wallenberg, GP-zones in Al-Zn-Mg alloys and their role in artificial aging, Acta Mater. 49 (2001) 3443-3451.

[7] X. Fan, D. Jiang, Q. Meng, Z. Lai, X. Zhang, Characterization of precipitation microstructure and properties of 7150 aluminium alloy, Mater. Sci. Eng. A 427(1-2) (2006) 130-135.

[8] P. Bai, X. Hou, X. Zhang, C. Zhao, Y. Xing, Microstructure and mechanical properties of a large billet of spray formed Al–Zn–Mg–Cu alloy with high Zn content, Mater. Sci. Eng. A 508(1-2) (2009) 23-27.

[9] A.C.U. Rao, V. Vasu, M. Govindaraju, K.V.S. Srinadh, Stress corrosion cracking behaviour of 7xxx aluminum alloys: A literature review, Trans. Nonferrous Met. Soc. China 26(6) (2016) 1447-1471.

[10] A. Lervik, J. C Walmsley, L. Lodgaard, C. D Marioara, R. Johnsen, O. Lunder, R. Holmestad, Stress corrosion cracking in an extruded Cu-free Al-Zn-Mg Alloy, Metals 10(9) (2020) 1194.

[11] A. Lervik, C.D. Marioara, M. Kadanik, J. Walmsley, B. Milkereit, R. Holmestad, Precipitation in an extruded AA7003 aluminium alloy: Observations of 6xxx-type hardening phases, Mater. Des. 186 (2020) 108204.

[12] J.B. Friauf, The crystal structure of magnesium di-zincide, Phys. Rev. 29(1) (1927) 34-40.

[13] Y. Komura, K. Tokunaga, Structural studies of stacking variants in Mg-base Friauf-Laves phases, Acta. Crystallogr. B 36(7) (1980) 1548-1554.

[14] T.-F. Chung, Y.-L. Yang, B.-M. Huang, Z. Shi, J. Lin, T. Ohmura, J.-R. Yang, Transmission electron microscopy investigation of separated nucleation and in-situ nucleation in AA7050 aluminium alloy, Acta Mater. 149 (2018) 377-387.

[15] T.-F. Chung, Y.-L. Yang, M. Shiojiri, C.-N. Hsiao, W.-C. Li, C.-S. Tsao, Z. Shi, J. Lin, J.-R. Yang, An atomic scale structural investigation of nanometre-sized η precipitates in the 7050 aluminium alloy, Acta Mater. 174 (2019) 351-368.

[16] D. Godard, P. Archambault, E. Aeby-Gautier, G. Lapasset, Precipitation sequences during quenching of the AA 7010 alloy, Acta Materialia 50(9) (2002) 2319-2329.

[17] G. Sha, A. Cerezo, Early-stage precipitation in Al–Zn–Mg–Cu alloy (7050), Acta Mater. 52(15) (2004) 4503-4516.

[18] A. Bendo, K. Matsuda, A. Lervik, T. Tsuru, K. Nishimura, N. Nunomura, R. Holmestad, C.D. Marioara, K. Shimizu, H. Toda, M. Yamaguchi, An unreported precipitate orientation relationship in Al-Zn-Mg based alloys, Mater. Charact. 158 (2019) 109958.

[19] G. Sha, Y.B. Wang, X.Z. Liao, Z.C. Duan, S.P. Ringer, T.G. Langdon, Influence of equal-channel angular pressing on precipitation in an Al–Zn–Mg–Cu alloy, Acta Mater. 57(10) (2009) 3123-3132.

[20] A.J. De Ardo, C.J. Simensen, A structural investigation of multiple aging of Al-7 wt pct Zn-2.3 wt pct Mg, Metall. Trans. 4(10) (1973) 2413-2421.

[21] V. Hansen, O.B. Karlsen, Y. Langsrud, J. Gjønnes, Precipitates, zones and transitions during aging of Al-Zn-Mg-Zr 7000 series alloy, Mater. Sci. Technol. 20(2) (2013) 185-193.

[22] B.A. Parker, The effect of certain trace element additions on the ageing behavior of an Aluminum-4 wt% Zinc-3 wt% Magnesium alloy, J Aust Inst Metals 17 (1972) 31-38.

[23] A. Bendo, K. Matsuda, S. Lee, K. Nishimura, N. Nunomura, H. Toda, M. Yamaguchi, T. Tsuru, K. Hirayama, K. Shimizu, H. Gao, K. Ebihara, M. Itakura, T. Yoshida, S. Murakami, Atomic scale HAADF-STEM study of η' and η_1 phases in peak-aged Al‑Zn‑Mg alloys, J. Mater. Sci. 53(6) (2017) 4598-4611.

[24] A. Bendo, T. Maeda, K. Matsuda, A. Lervik, R. Holmestad, C.D. Marioara, K. Nishimura, N. Nunomura, H. Toda, M. Yamaguchi, K.-i. Ikeda, T. Homma, Characterisation of structural

similarities of precipitates in Mg–Zn and Al–Zn–Mg alloys systems, Philos. Mag. 99(21) (2019) 2619-2635.

[25] C.D. Marioara, W. Lefebvre, S.J. Andersen, J. Friis, Atomic structure of hardening precipitates in an Al–Mg–Zn–Cu alloy determined by HAADF-STEM and first-principles calculations: relation to η-MgZn$_2$, J. Mater. Sci. 48(10) (2013) 3638-3651.

[26] F. Cao, J. Zheng, Y. Jiang, B. Chen, Y. Wang, T. Hu, Experimental and DFT characterization of η' nano-phase and its interfaces in Al Zn Mg Cu alloys, Acta Mater. 164 (2019) 207-219.

[27] B. Cheng, X. Zhao, Y. Zhang, H. Chen, I. Polmear, J.-F. Nie, Co-segregation of Mg and Zn atoms at the planar η_1-precipitate/Al matrix interface in an aged Al–Zn–Mg alloy, Scr. Mater. 185 (2020) 51-55.

[28] L. Jones, H. Yang, T.J. Pennycook, M.S. Marshall, S. Van Aert, N.D. Browning, M.R. Castell, P.D. Nellist, Smart Align—a new tool for robust non-rigid registration of scanning microscope data, Adv. Struct. Chem. Imaging 1(1) (2015) 1-16.

[29] J. G. Kresse, Furthmüller, Efficient iterative schemes for ab initio total-energy calculations using a plane-wave basis set, Phys. Rev. B 54 (1996) 11169-11186.

[30] P.E. Blöchl, Projector augmented-wave method, Phys. Rev. B 50(24) (1994) 17953-17979.

[31] G. Kresse, D. Joubert, From ultra-soft pseudo-potentials to the projector augmented wave method, Phys. Rev. B 59 (1999) 1758.

[32] P. Vinet, J.H. Rose, J. Ferrante, J.R. Smith, Universal features of the equation of state of solids, J. Phys. Condens. Matter 1 (1989) 1941.

[33] D.M. Ceperley, B.J. Alder, Ground state of the electron gas by a stochastic method, Phys. Rev. Lett. 45(7) (1980) 566-569.

[34] J.P. Perdew, A. Zunger, Self-interaction correction to density-functional approximations for many-electron systems, Phys. Rev. B 23(10) (1981) 5048-5079.

[35] G. Simmons, H. Wang, Single crystal elastic constants and calculated aggregate properties: a handbook, M. I. T. Press, Cambridge, MA (1971).

[36] J.P. Perdew, K. Burke, M. Ernzerhof, Generalized gradient approximation made simple, Phys. Rev. Lett. 77 (1996) 3865.

[37] M.M. Treacy, Z dependence of electron scattering by single atoms into annular dark-field detectors, Microsc. Microanal. 17(6) (2011) 847-58.

[38] C. Zhang, Y. Jiang, F. Cao, T. Hu, Y. Wang, D. Yin, Formation of coherent, core-shelled nano-particles in dilute Al-Sc-Zr alloys from the first-principles, J. Mater. Sci. Technol. 35(5) (2019) 930-938.

[39] T. Tsuru, M. Yamaguchi, K. Ebihara, M. Itakura, Y. Shiihara, K. Matsuda, H. Toda, First-principles study of hydrogen segregation at the $MgZn_2$ precipitate in Al-Mg-Zn alloys, Comput. Mater. Sci. 148 (2018) 301-306.

[40] L. Yang, Y. Jiang, Y. Wu, G.R. Odette, Z. Zhou, Z. Lu, The ferrite/oxide interface and helium management in nano-structured ferritic alloys from the first principles, Acta Mater. 103 (2016) 474-482.

[41] J.R. Smith, Y. Jiang, A.G. Evans, Adhesion of the γ-Ni (Al)/α-Al$_2$O$_3$ interface: a first-principles assessment, Int. J. Mater. Res. 98(12) (2007) 1214-1221.

[42] Y. Jiang, J.R. Smith, A.G. Evans, First principles assessment of metal/oxide interface adhesion, Appl. Phys. Lett. 92(14) (2008) 141918.

[43] S. Hirosawa, F. Nakamura, T. Sato, First-principles calculation of interaction energies between solutes and/or vacancies for predicting atomistic behaviors of microalloying elements in aluminum alloys, Mater. Sci. Forum 561-565 (2007) 283-286.